Structural and physical properties of trilayer nickelates $R_4Ni_3O_{10}$ (R = La, Pr, and Nd)

Dibyata Rout,[1] Sanchayeta Ranajit Mudi,[1] Marco Hoffmann,[2] Sven Spachmann,[2] Rüdiger Klingeler,[2,3] and Surjeet Singh[1,4,*]

[1]*Department of Physics, Indian Institute of Science Education and Research, Pune, Maharashtra-411008, India*
[2]*Kirchhoff Institute of Physics, Heidelberg University, INF 227, D-69120, Heidelberg, Germany*
[3]*Centre for Advanced Materials (CAM), Heidelberg University, INF 225, D-69120, Heidelberg, Germany*
[4]*Center for Energy Science, Indian Institute of Science Education and Research, Pune, Maharashtra-411008, India*

(Received 9 July 2020; revised 30 September 2020; accepted 2 November 2020; published 24 November 2020)

We investigate in detail the low-temperature structural and physical properties of the trilayer nickelates $R_4Ni_3O_{10}$ (R = La, Pr, and Nd), which crystallize with a monoclinic symmetry (space group $P2_1/a$, $Z = 4$) and undergo a metal-to-metal transition (MMT) near T_{MMT}= 135 K (La), 156 K (Pr), and 160 K (Nd). Using a high-resolution synchrotron powder x-ray diffraction technique, we show that the lattice parameters in all cases exhibit an anomalous behavior at T_{MMT}, however, without any sign of change in the lattice symmetry. Unambiguous signature of MMT is also observed in the magnetic and transport data, suggesting a strong coupling between the electronic, magnetic, and structural degrees of freedom. Analysis of thermal expansion yields hydrostatic pressure dependence of MMT in close agreement with previous high-pressure experiments. In $Pr_4Ni_3O_{10}$, the Pr^{3+} ions located in the rocksalt (RS) layers order magnetically near 5 K, which is significantly suppressed compared to $\theta_p \sim -36$ K. In contrast, Pr^{3+} ions in the perovskite-block (PB) layers exhibit a crystal field (CF) induced nonmagnetic singlet ground state. In $Nd_4Ni_3O_{10}$, on the other hand, the CF ground state of Nd^{3+} ions in both RS and PB layers is a Kramers doublet. The heat capacity of $Nd_4Ni_3O_{10}$ shows a pronounced Schottky-like anomaly near 40 K, and a sharp upturn indicating short-range correlations between the Nd-moments below 10 K. However, no signs of long-range ordering of Nd-moments could be found down to 2 K despite a sizable value of $\theta_p \sim -40$ K. The strongly suppressed magnetic long-range ordering in both R = Pr and Nd suggests the presence of strong magnetic frustration in these compounds. In the presence of an overwhelming Schottky contribution, the electronic term in the specific heat of $Pr_4Ni_3O_{10}$ and $Nd_4Ni_3O_{10}$ appears highly inflated, which can be *falsely* interpreted as a sign of heavy fermion behavior as is done in a recent study on $Nd_4Ni_3O_{10}$. Accordingly, the low-temperature resistivity of these compounds is found to follow a $-T^{0.5}$ rather than a $-\ln T$ dependence.

DOI: 10.1103/PhysRevB.102.195144

I. INTRODUCTION

Transition-metal oxides based on nickel, or nickelates for short, have witnessed a resurgence of interest in the last few years. Several recent papers have shown that nickelates are unique due to their strongly coupled charge, spin, and lattice degrees of freedom, which can be manipulated to engineer interesting electronic and magnetic phases (see, for example, Refs. [1–3]). Another reason for this resurgence could be attributed to the discovery of superconductivity in $Nd_{0.8}Sr_{0.2}NiO_2$ by Li *et al.* in the year 2019, which, in fact, led to the fulfillment of a long-sought-after quest for superconductivity in the nickelates [4]. Nearly two years before this momentous discovery, an Angle Resolved Photoemission Spectroscopy (ARPES) study on single crystals of $La_4Ni_3O_{10}$, which is the $n = 3$ member of the Ruddlesden Popper (RP) $La_{n+1}Ni_nO_{3n+1}$ ($n = 1, 2, 3 \ldots \infty$) series, revealed a large hole Fermi surface that closely resembles the Fermi surface of optimally hole-doped cuprates [5] (see also Ref. [6]). This discovery is even more significant since the infinite layer $NdNiO_2$ (called the T' phase) is related to the perovskite $NdNiO_3$ ($n = \infty$ member of RP series), from which it is obtained by a process of chemical reduction. In general, there is a whole range of infinite layer T' phases given by $R_{n+1}Ni_nO_{2n+2}$ ($n = 1, 2, 3 \ldots \infty$), where R is usually an alkaline earth or rare-earth ion, that are analogously related to their corresponding RP $R_{n+1}Ni_nO_{3n+1}$ phases. The nickelates of the RP series, therefore, constitute the primary phases with perovskite-type structure elements from which other nickelates, including the infinite layer T' variants, can be derived.

A survey of past literature reveals that excluding $n = \infty$ (i.e., $RNiO_3$ where R is a tripositive rare-earth ion), the $n = 1, 2, 3 \ldots$, members of the $R_{n+1}Ni_nO_{3n+1}$ family are relatively much less investigated [7,8]. The intermediate members between $n = 1$ and $n = \infty$ exhibit a mixed-valent phase, ranging from 2+ for $n = 1$ to 3+ for $n = \infty$. Such a mixed valency is well-known to give rise to strongly coupled electronic and magnetic phases (see, for example, Ref. [10]). Hence, there is a significant interest to study them in the recent years.

In this regards, the $n = 3$ member of the RP series, consisting of the compounds $R_4Ni_3O_{10}$ (R = La, Pr and Nd) with an

*surjeet.singh@iiserpune.ac.in

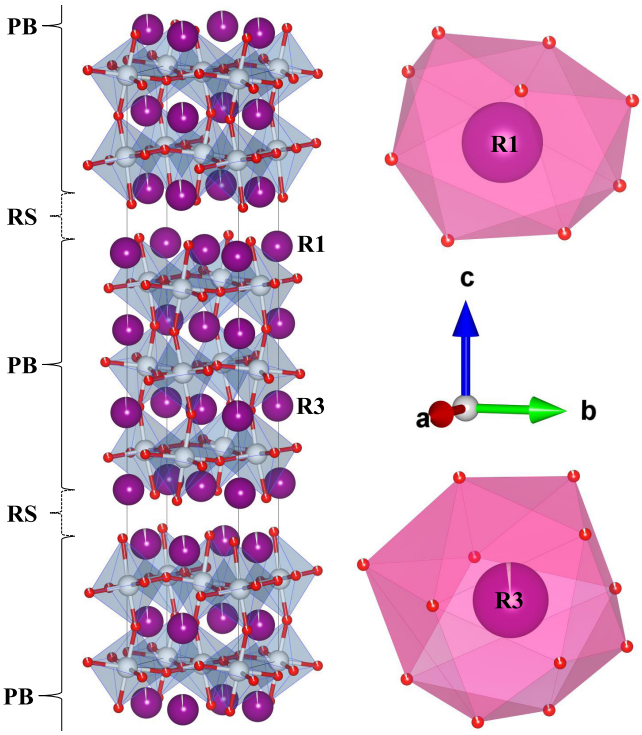

FIG. 1. The crystal structure of trilayer $R_4Ni_3O_{10}$ (R = La, Pr, and Nd) nickelates. Here PB represents the perovskite block layers and RS represents the rocksalt layers. R1 and R3 denote ninefold and 12-fold coordinated rare-earth ions located in RS and PB layers, respectively.

average Ni valence of 2.67, will be interesting to investigate (see Fig. 1 for the crystal structure). They are relatively easy to synthesize in pure form, and, if needed, can readily be reduced to their corresponding infinite layer T' analogs. Previous studies have shown that they undergo a metal-to-metal transition (MMT) in the temperature range 135 K to 160 K depending on the identity of the R ion.

Recently, these trilayer nickelates have attracted a great deal of attention (see, for example, Refs. [5,11–16]). However, the majority of previous studies have mainly focused on understanding the nature of MMT where Ni $3d$ electrons play a crucial role. The magnetic ground state of rare-earth sublattice or of the $4f$ electrons and the interplay between $3d$ and $4f$ electrons have not been studied in detail so far. Moreover, the question of whether there is a structural phase transition associated with MMT or not has remained an unsettled issue over the years.

Here, we investigate the resistivity, thermopower, thermal conductivity, magnetic susceptibility, and specific heat of $R_4Ni_3O_{10}$ (R = La, Pr, and Nd) in considerable detail to explore and understand the low-temperature properties arising due to $4f$ electrons. Further, to throw light on the nature of MMT, the crystal structure of $R_4Ni_3O_{10}$ (R = La, Pr, and Nd) is examined over a broad temperature range, spanning MMT in all three compounds using a very high-resolution synchrotron data on high-quality samples. This is complemented by high-resolution capacitance dilatometry to investigate the temperature dependence of thermal expansion and Grüneisen parameter across the MMT.

We show that in $Pr_4Ni_3O_{10}$, the Pr ions in the rocksalt (RS) block layers undergo a magnetic ordering near T_N = 5 K while the Pr^{3+} ions in the perovskite block (PB) layers exhibit a crystal-field split nonmagnetic singlet ground state. On the other hand, Nd^{3+} moments in $Nd_4Ni_3O_{10}$ show no long-range ordering down to 2 K (lowest temperature in our measurements). The paramagnetic Curie temperatures for these compounds is found to be of the order of −40 K, indicating the presence of strong magnetic frustration. The effective carrier mass deduced from specific heat and thermopower lies in the range of two to four times the free electron mass, indicating moderately enhanced electronic correlations. The resistivities of all three compounds show an upturn at low temperatures, obeying a $-\sqrt{T}$ dependence. No evidence for the Kondo effect or heavy Fermion behavior in any of these compounds could be found, contradicting the claim of a heavy fermion state due to Ni^{3+}-centered Kondo effect in $Nd_4Ni_3O_{10}$ published recently [13].

The rest of the paper has been organized as follows: The details of the experimental methods are given in Sec. II. This is followed by Results and Discussion in Sec. III, which has been further divided into several subsections for convenience. The details of the crystal structure appear under Sec. III A. The electrical and thermal transport and the magnetic susceptibility are briefly discussed in Sec. III B. This is followed by subsections on specific heat (Sec. III C) and thermal expansion (Sec. III D), both of which form the crux of the paper. Finally, a summary of the important results and conclusions drawn are presented under Sec. IV.

II. EXPERIMENTAL DETAILS

Conventional solid-state synthesis of higher members of the RP family leads to the formation of mixed phases and intergrowth [17,18], which greatly influences the physical properties of these compounds. Hence, we adopted a wet chemical method to synthesize these compounds in a pure phase. Further details of sample preparation are given in Ref. [19]. The phase purity was monitored using a Bruker D8 Advance powder x-ray diffractometer. The chemical composition of the samples was analyzed using the energy dispersive x-ray analysis technique in a Zeiss Ultra Plus scanning electron microscope. Since the structural and electronic properties of RP phases often show strong dependence on the oxygen stoichiometry, we carried out complete decomposition of our samples under a 10% Ar-H_2 atmosphere, employing a heating rate of 5 K/min in a high-resolution Thermogravometric analysis (TGA) setup (Netzsch STA 449 F1) from where we inferred the oxygen stoichiometry to lie in the range 97% to 98% of the ideal value for all the samples [19].

The high-resolution synchrotron powder x-ray diffraction experiments were carried out at the MSPD-BLO4 beamline of the ALBA synchrotron center, Barcelona, Spain. The samples were prepared in the form of finely ground powders that were placed in a borosilicate capillary tube of 0.5-mm inner diameter. The sample was cooled using an Oxford Cryostream 700 series nitrogen blower, and the diffractograms were collected in the range $0^o \leqslant 2\theta \leqslant 30^o$ with a step size of 0.003^o. The incident beam energy was set at 38 KeV (λ = 0.3263 Å) and

a high resolution MAD26 detector with an angular resolution of about 4×10^{-4} was used to resolve any subtle structural modifications [20]. The data at each temperature was collected at a rate of 30 min/scan. The structural refinement was done by the Rietveld method using the FULLPROF suite [21]. During the refinement, the occupancies of the O sites are fixed as fully occupied as x-ray diffraction is not sensitive to the position of lighter elements. The Pseudo-Voigt function was used to model the line profile. The linear interpolation method was used to define the background. To account for the anisotropic strain broadening of the peaks, the broadening model (quartic form) was used. In this model, only certain *hkl*-dependent strain parameters (S_{hkl}) were refined corresponding to the Laue class used. Further details are given in the Supplemental Material [19]. The quality of the refinement was assessed, both from the visual inspection of the fitted pattern or the difference plot, and the quantitative assessment on the basis of χ^2 and the *R* factors (R_{WP}, R_{EXP}, and R_P). For fitting the low-temperature data, the lattice parameters were refined along with angle β, the overall isotropic displacement factor (B_{iso}), and the strain coefficients.

Magnetization, resistivity, thermopower, and specific-heat measurements were done using a Physical Property Measurement System (PPMS), Quantum Design USA. Magnetization measurements were done both under the zero-field-cooled and field-cooled conditions. Resistivity measurements were done on sintered rectangular samples of known dimensions using the four-probe method. Gold wires were used for electrical contacts with silver conducting paste. Specific-heat measurements were performed using the relaxation method. The heat capacity of the sample holder and APIEZON N grease (addenda) was determined prior to the measurements.

The relative length changes dL/L were studied on cuboid-shaped sintered samples of approximate dimensions $3 \times 2 \times 1\,\mathrm{mm}^3$. The measurements were done in zero magnetic field by means of a three-terminal high-resolution capacitance dilatometer [22]. The relative volume changes $dV/V = 3dL/L$ and the volume thermal expansion coefficient $\beta = 3\alpha$, with $\alpha = 1/L \times dL(T)/dT$ are derived.

III. RESULTS AND DISCUSSION

A. Crystal structure

1. $La_4Ni_3O_{10}$

There is a great deal of ambiguity in previous literature regarding the space group that correctly defines the crystal structure of $La_4Ni_3O_{10}$. The earliest work by Seppänen *et al.* reported an orthorhombic space group *Fmmm* [23]. However, Tkalich *et al.* [24] and Voronin *et al.* [25] used the space group *Cmca*. Ling *et al.* [26], on the other hand, found the orthorhombic space group *Bmab* (unconventional setting for *Cmca*) to be more suitable for refining their neutron powder diffraction data. Zhang *et al.* carried out structural refinement on the powders obtained by crushing high-pressure floating-zone grown single crystalline specimens [15]. They propose that $La_4Ni_3O_{10}$ crystallizes in a mixture of *Bmab* and $P2_1/a$—the phase fraction between the two phases being a function of the cooling condition employed [15]. Finally, in a recent synchrotron based study by Kumar *et al.*, the space-group symmetry $P2_1/a$, $Z = 4$ has been endorsed [27].

To find the most appropriate space group from among those that were previously reported, we started by refining the structure using one space group at a time. To avoid biasing this procedure, every space group is tried till the refinement could not be improved further. Using this procedure (see Supplemental Material for details [19]), we found that $P2_1/a$ (space group No. 14, $Z = 4$) best fits the experimental data. However, even with $P2_1/a$, the calculated profile around the high intensity peaks in the range $2\theta = 6^\circ$ to 7°, and those around $2\theta = 9.7^\circ$, remains far from perfect as shown in the Supplemental Material [19]. In Ref. [27] also a similar difference between the calculated and measured intensities can also be seen (see Figs. 2*a* and 2*b* of Ref. [27]).

We therefore attempted a mixed phase refinement wherein, besides the principal $P2_1/a$ phase, two additional phases, (i) the orthorhombic *Bmab* (SG No. 64) phase and (ii) a lower ($n = 2$) member $La_3Ni_2O_7$, with an orthorhombic space group *Cmcm* (SG No. 63), are also incorporated. As shown in the Supplemental Material [19], inclusion of the *Bmab* phase alone improves the quality of fit significantly with $P2_1/a : Bmab \equiv 86.3 : 13.7$. To see if we can get an even better match with the observed intensities, $La_3Ni_2O_7$ was also incorporated which lead to a further slight improvement. In this case, we find the ratio of three phases to be $P2_1/a : Bmab : La_3Ni_2O_7 \equiv 85.6 : 7.8 : 6.6$. Clearly, in both two- and three-phase refinements, the phase fraction of the primary phase $P2_1/a$ remains more or less unchanged. Since the *R* factors quantifying the quality of fit are slightly lower for the three-phase refinement, here we have shown the results for the same in Fig. 2(a1). Finally, even in the three-phase refinement, some mismatch between the observed and calculated intensity around $2\theta = 10^\circ$ remains; this has also been reported in previous studies and may arise from stacking faults [28]. It should also be remarked that a small extra peak, ~1% of the intensity of the main peak, near $2\theta = 8.95^\circ$, is also observed [see Figs. 3(b), 3(f), or 3(j)], which indicates the presence of a small unidentified parasitic phase.

Figures 2(b1)–2(f1) show the temperature variation of the lattice parameters of the $P2_1/a$ phase. The lattice parameters decrease monotonically upon cooling, exhibiting a clearly discernible anomaly at T_{MMT}. The *b* axis, in fact, undergoes an expansion upon further cooling below T_{MMT}. The diffraction patterns recorded below T_{MMT} however revealed neither the appearance of any new diffraction peak nor any peak splitting, which suggests that the structural reorganization across the MMT, if any, is rather subtle without any noticeable change of the lattice symmetry (see Fig. 3). The negative thermal expansion along the *b* axis is in agreement with that reported by Kumar *et al.* (Ref. [27]). The temperature variation of angle β, shown in Fig. 2(e1), shows an increasing behavior upon cooling with a perceptible dip at T_{MMT}. For comparison, the normalized lattice parameters are shown in Fig. 2(g1).

2. $Pr_4Ni_3O_{10}$

Figure 2(a2) shows the results of Rietveld refinement for $Pr_4Ni_3O_{10}$. In this case, the refinement was done using the monoclinic space group $P2_1/a$ (SG No. 14, $Z = 4$) alone,

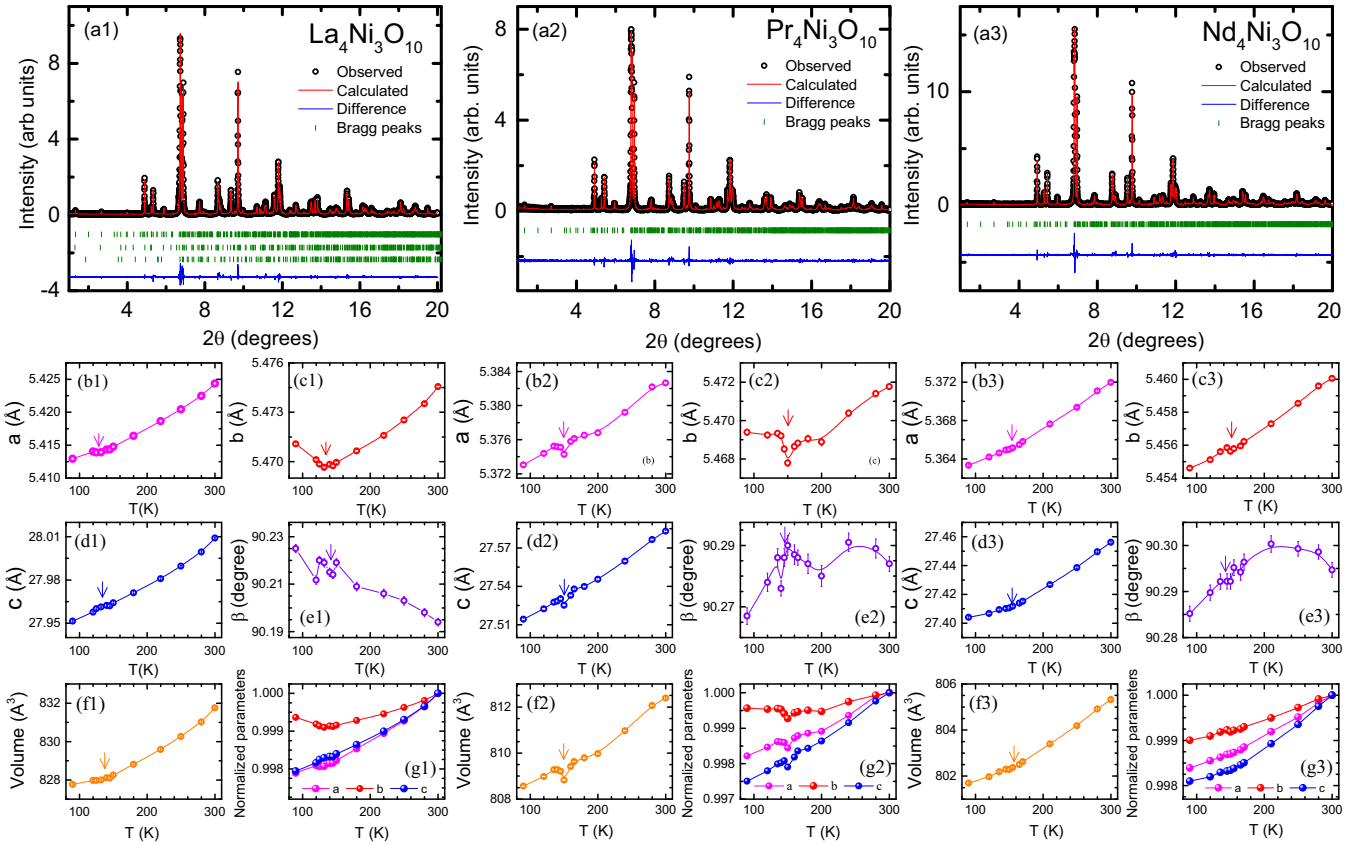

FIG. 2. Rietveld refinement results of the room-temperature synchrotron powder x-ray diffraction data for the three nickelates: (a1) $La_4Ni_3O_{10}$, (a2) $Pr_4Ni_3O_{10}$, (a3) $Nd_4Ni_3O_{10}$. The black circles represent observed data (Y_{obs}), the red lines are the calculated intensity (Y_{calc}), and the vertical green bars indicate the positions of the Bragg peaks; the blue line at the bottom is the difference plot ($Y_{obs} - Y_{calc}$). In panel (a1), the first, second, and third rows of Bragg peaks correspond to $P2_1/a$, *Bmab*, and $La_3Ni_2O_7$ phases, respectively. In panels (a2) and (a3), only single phase refinement is done and the Bragg peaks are for $P2_1/a$. Panels (b)–(d) show the temperature variation of lattice parameters; panels (e), (f) show the temperature dependence of angle β and unit cell volume, respectively; (g) panels show the normalized unit cell parameters. In some cases, the size of the error bar is smaller than that of the data points.

which resulted in a satisfactory fit except near the highest intensity peak, where the calculated profile does not exactly match the observed data. Inclusion of strain improved the fitting to some extent but did not resolve the issue completely. Similar inconsistency over the same 2θ range has also been previously observed [15]. Whether the stacking faults or the intergrowth of lower RP members is the reason could not, however, be reliably ascertained. Also, analogous to $La_4Ni_3O_{10}$, some intensity mismatch is observed near $2\theta = 10^\circ$ (peak $\bar{2}21$), which may be due to the stacking faults [28].

As shown in Figs. 2(b2)–2(e2), in the temperature range around 156 K, where MMT is expected to occur, a clear anomaly in the lattice parameters is observed. The *b*-axis parameter shows an increase upon cooling below the MMT, analogous to $La_4Ni_3O_{10}$. In the temperature dependence of angle β, an appreciable nonmonotonic variation has also been observed between the MMT and room temperature.

3. $Nd_4Ni_3O_{10}$

Figure 2(a3) shows the results of Rietveld refinement for $Nd_4Ni_3O_{10}$ at room temperature. The structural refinement in this case too is done using the monoclinic space group $P2_1/a$ (SG No. 14; $Z = 4$) alone. Though all the observed peaks could be satisfactorily accounted for, the highest intensity peak was found to be unusually broad and strain model 2 is used to account for it (see Sec. II).

As shown in Figs. 2(b3)–2(e3), the lattice parameters of $Nd_4Ni_3O_{10}$ decrease monotonically upon cooling with a weak anomaly around 160 K, which coincides with T_{MMT} previously reported for this compound. This anomaly is most prominent in the variation of the *b* parameter. However, unlike $La_4Ni_3O_{10}$ and $Pr_4Ni_3O_{10}$, the *b* parameter in this case continues to decrease upon cooling below the MMT. The temperature variation of angle β is shown in Fig. 2(e3). Upon cooling below room temperature, β first increases down to about $T = 200$ K and decreases upon further cooling, showing a broad peak near $T = 200$ K which may indicate the presence of a rather continuous but subtle and nonmonotonic structure evolution occurring even above the MMT, analogous to the case of $Pr_4Ni_3O_{10}$. However, this should be further confirmed by collecting data at intermediate temperatures for all the samples.

Table I summarizes the refinement details for the room-temperature crystal structure of $R_4Ni_3O_{10}$, R = La, Pr, and Nd. The room-temperature lattice parameters agree well with the values reported in previous literature [27,29,30]. The crystal structure of $R_4Ni_3O_{10}$ (monoclinic $P2_1/a$, $Z = 4$),

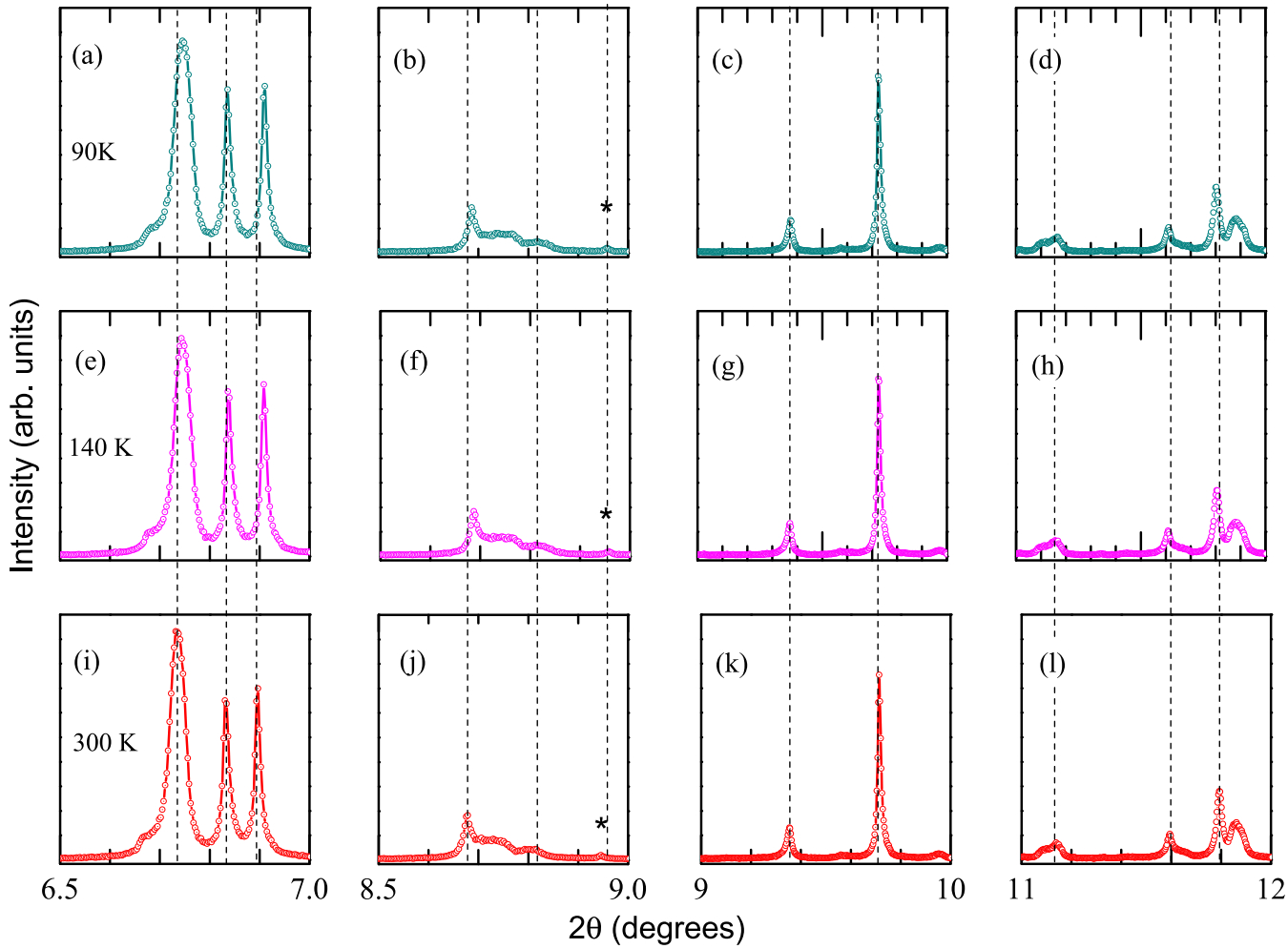

FIG. 3. Synchrotron powder x-ray diffraction data for $La_4Ni_3O_{10}$ at three representative temperatures: 90 K (top row), 140 K (middle row), and 300 K (bottom row) over select 2θ ranges. The dashed vertical lines are shown as a guide to the eye. The y scale in each panel is kept the same. Asterisk indicates an unidentified peak. Analogous low-temperature data for $Pr_4Ni_3O_{10}$ and $Nd_4Ni_3O_{10}$ are shown in the Supplemental Material [19].

shown in Fig. 1, comprises triple PB layers $(RNiO_3)_3$, which consist of corner-linked NiO_6 octahedra. These triple PB layers are separated by RO layers with the RS structure. There are four inequivalent $R-$atoms, two of these are located within the PB layers ($R3$, $R4$). They have a deformed12-fold coordination analogous to the perovskites $RNiO_3$ as shown in Fig. 1. The remaining two R atoms are located within the RS layers ($R1$, $R2$) with a ninefold coordination. Likewise, there are four distinct crystallographic sites for the Ni atoms. Borrowing the terminology used in Ref. [30], we shall label them as Ni1, Ni2: located in the inner layer (IL), and Ni3, Ni4: located in the outer layer (OL) that faces the RO layer on one side and PB layer on the other. The various R–O and Ni–O bond distances for all three samples are given in the Supplemental Material [19]. In all three cases, the elongated Ni–O bonds are apical, pointing toward the RS layer which was previously speculated to be a consequence of Ni^{3+}(OL)–Ni^{2+}(IL) charge ordering [30].

TABLE I. Refinement parameters obtained using the high-resolution synchrotron data for room-temperature crystal structure of $R_4Ni_3O_{10}$ (R = La, Pr, and Nd). The error bars are shown in the parenthesis.

Specimen	Space group	SG No.	Phase type	Phase %	a(Å)	b(Å)	c(Å)	β	χ^2	R_{WP}	R_{EXP}	R_P
$La_4Ni_3O_{10}$	$P2_1/a$	14	M[a]	85.6	5.4243(5)	5.4748(5)	28.0053(4)	90.192^o(3)	6.15	14.7	5.90	11.7
	Bmab	64	O[a]	7.8	5.4040	5.4621	28.5542	90^o				
	Cmcm	63	O[a]	6.6	20.1250	5.4638	5.4638	90^o				
$Pr_4Ni_3O_{10}$	$P2_1/a$	14	M[a]	100	5.3826(4)	5.4717(4)	27.583(4)	90.284^o(3)	3.86	19.0	9.67	16
$Nd_4Ni_3O_{10}$	$P2_1/a$	14	M[a]	100	5.3719(4)	5.46(5)	27.4560(4)	90.299^o(3)	4.57	15.8	7.41	12.7

[a]M†: monoclinic and O†: orthorhombic.

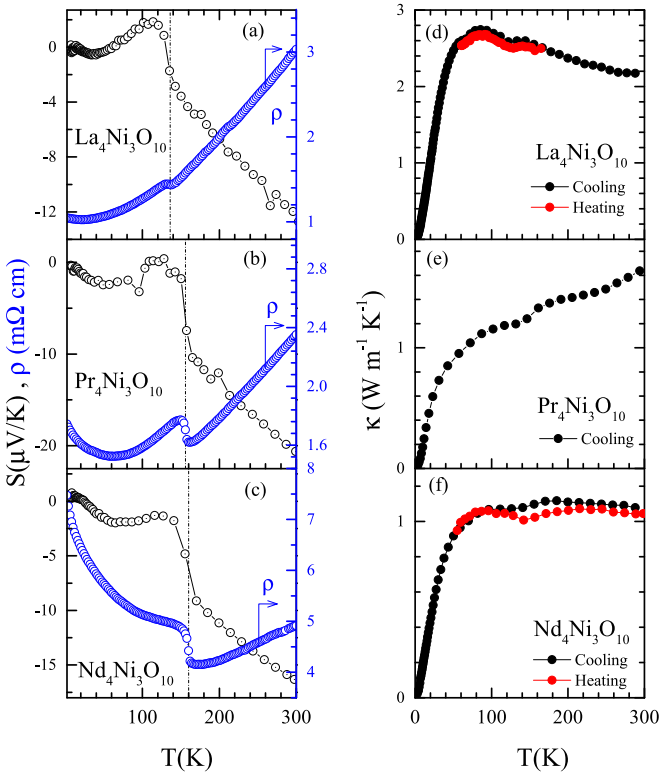

FIG. 4. Panels (a)–(c) show the temperature variation of resistivity (ρ) and thermoelectric power (S) for $La_4Ni_3O_{10}$, $Pr_4Ni_3O_{10}$, and $Nd_4Ni_3O_{10}$, respectively. The temperature variation of their thermal conductivity (κ) is shown, respectively, in (d)–(f).

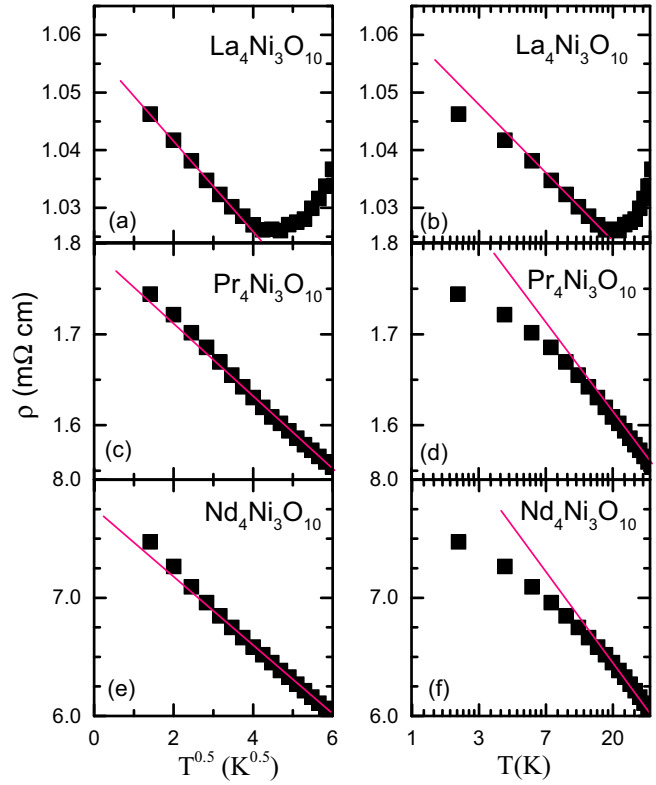

FIG. 5. Temperature (T) variation of resistivity (ρ) of the three nickelates shown on $T^{0.5}$ scale (left panels), and ln T scale (right panels). The straight lines are guide to the eye drawn to compare the agreement of the observed data with the two proposed behaviors. The slight departure from linearity at low-temperatures in Pr (c) and Nd (e) samples for $T^{0.5}$ scaling is possibly related to the short-range ordering of the rare-earth moments as discussed in the text.

B. Transport and magnetization

1. Resistivity

Figure 4 shows the temperature dependence of resistivity (ρ), thermopower (S), and thermal conductivity (κ) for all three samples. We first examine the electrical resistivity. Upon cooling below room temperature, $\rho(T)$ for all three samples decreases monotonically down to a temperature of approximately 136 K (La), 156 K (Pr), and 160 K (Nd). Upon further cooling, ρ increases in a steplike fashion, which can be identified with the MMT. The temperature at which the step occurs ($T_{\rm MMT}$) agrees well with the temperature where the lattice parameters show an anomaly. The resistivity discontinuity ($\Delta\rho$) at $T_{\rm MMT}$ appears to be first-order-like, however, no measurable thermal hysteresis at $T_{\rm MMT}$ could be observed between the heating and cooling data.

Below the MMT, the resistivity for $La_4Ni_3O_{10}$ and $Pr_4Ni_3O_{10}$ continue to decrease down to some temperature T_0, which is followed by an upturn or a region of negative $d\rho/dT$ that persists down to 2 K. T_0 is $\simeq$20 K and $\simeq$80 K for $La_4Ni_3O_{10}$ and $Pr_4Ni_3O_{10}$, respectively. These observations concerning the behavior of $\rho(T)$ in the La and Pr compounds are in good agreement with previous reports [13,27,29,31]. In $Nd_4Ni_3O_{10}$, however, $d\rho/dT \simeq 0$ down to about 100 K, followed by a steep upturn at lower temperatures. In previous resistivity data, however, before the low-temperature upturn, a region of negative $d\rho/dT$ is shown [13,32]. Such variations can arise due to slight differences in the oxygen off-stoichiometry between the various samples, assuming that other factors, such as purity and density, are the same [29]. Typically, the extent of oxygen off-stoichiometry is controlled by the synthesis protocol. The $Nd_4Ni_3O_{10}$ sample used in Ref. [13] was reported to have been prepared under a pressurized oxygen atmosphere of 5 bar at 1100 °C for 24 h. Similarly, in Ref. [32], the sample was prepared by annealing it under an oxygen flow for a period of close to 120 h as opposed to 24 h in our case. From the TGA data (Fig. 1 of the Supplemental Material [19]), it is clear that our Nd sample is oxygen deficient with $O_{9.8}$ as its oxygen content instead of full O_{10}. The exact oxygen off-stoichiometry for the samples used in Refs. [13,32] is not known.

In previous studies, this low-temperature resistivity upturn has been variously interpreted. While it is attributed to the weak localization due to inelastic electron-electron interactions in $La_4Ni_3O_{10}$ [27], the Kondo effect was claimed to be the reason in $Nd_4Ni_3O_{10}$ [13]. To resolve this issue, we replotted the low-temperature data for all three compounds on two different temperature scales: (i) $T^{0.5}$ and (ii) ln T. The results are shown in Fig. 5. Clearly, the data for all three samples are best described by a $-\sqrt{T}$ dependence which persists down to the lowest temperature of 2 K. The very slight departure

from this scaling for $Pr_4Ni_3O_{10}$ and $Nd_4Ni_3O_{10}$ near 10 K can be attributed to the short-range ordering of the rare-earth moments (*vide infra*). On the contrary, the $-\ln T$ behavior does not describe the upturn in ρ satisfactorily or does so only over a narrow temperature range, with significant departure at low temperatures. Attempts to fit the low-temperature upturn to the Arrhenius or variable range hopping models (with or without interactions) also did not give satisfactory results (not shown). The analysis above clearly favors a $-\sqrt{T}$ dependence over other functional dependencies commonly used to describe the low-temperature upturn in resistivity. The validity of $-\sqrt{T}$ behavior suggests that at low temperatures, weak localization due to inelastic electron-electron scattering is possibly what causes the resistivity upturn in all three compounds, which is a typical characteristic of disordered metals and alloys [33]. Here, the structural disorder might be in the form of stacking faults and intergrowth whose presence is reflected in the powder x-ray diffraction. This conclusion is also in agreement with Ref. [27]. On the other hand, the evidence for the Kondo effect in our data is rather weak.

2. Thermopower

The thermopower of these samples is shown in Figs. 4(a)–4(c). The overall behavior and range of variation of S for the three samples is comparable to that previously reported [29,34]. The temperature variation of S parallels that of ρ in the sense that at T_{MMT}, $S(T)$ exhibits a sharp jump, which can be understood based on the Mott's formula for thermopower, which is given by

$$S = \frac{\pi^2}{3}\frac{k_B^2 T}{e}\left(\frac{\partial \ln \sigma(E)}{\partial E}\right)_{E=E_F}, \tag{1}$$

where k_B is the Boltzmann constant, $\sigma(E)$ is the electrical conductivity, e the electronic charge, and E_F is the Fermi energy. Since, σ can be expressed as $\sigma = n(E)q\mu(E)$, where $n(E) = D(E)f(E)$: $D(E)$ being the density of states, and $f(E)$ the Fermi-Dirac distribution function, and μ is the carrier mobility; one can rewrite Eq. (1) with a term in S proportional to the quantity dn/dE at E_F, i.e., change in carrier concentration with respect to energy at E_F, which is expected to vary drastically due to the opening of a gap at E_F below the MMT as shown in previous ARPES studies [5].

We notice that, for $T > T_{MMT}$, $|S|$ increase almost linearly with increasing temperature, as is typically seen for metals. Naively, one can use the single parabolic band model approximation to rewrite the Mott formula in Eq. (1) in the following form:

$$S = \frac{8\pi^2 k_B^2 m^*}{3eh^2}\left(\frac{\pi}{3n}\right)^{\frac{2}{3}} T, \tag{2}$$

where m^* is the band effective mass of the charge carriers. By fitting S above T_{MMT} using $S = a_o T$, where a_0 is the prefactor in Eq. (2), one can estimate m^*. For this purpose, we use n obtained from the Hall coefficient $R_H \approx 10^{-3}\text{cm}^3/\text{C}$ at $T = 300$ K [35]. Following this procedure, we get $m^* \approx 3.0m_0$ for $La_4Ni_3O_{10}$, $\approx 3.7m_0$ for $Pr_4Ni_3O_{10}$, and $\approx 2.7m_0$ for $Nd_4Ni_3O_{10}$.

3. Thermal conductivity

The temperature variation of thermal conductivity (κ) is shown in Figs. 4(d)–4(f). For all three samples, the T_{MMT} is manifested in κ as a small but clearly discernible kink. For R = La and Pr, we measured the data both while heating and cooling and found some hysteresis around T_{MMT}. However, since no hysteresis was found in ρ, it is difficult to conclude if this is an intrinsic feature or a measurement issue. At low temperatures, κ increases upon heating as $\sim T^3$, which suggests that in this temperature range the acoustic phonons contribute dominantly to κ. Upon further heating, a noticeable change in the functional form of κ takes place for $T \gtrsim 50$ K: In $La_4Ni_3O_{10}$, κ shows a broad peak in the range from 50 K to 100 K with a peak value of $3\,\text{Wm}^{-1}\text{K}^{-1}$ around 80 K; in $Pr_4Ni_3O_{10}$, κ shows an increasing behavior all the way up to 300 K, albeit with a much slower rate for $T \gtrsim 50$ K; and, in $Nd_4Ni_3O_{10}$, κ gradually levels off with a saturated value of $\approx 1\ \text{W m}^{-1}\text{K}^{-1}$ for $T > 100$ K. Thus, the behavior of κ in all three cases is rather similar at low temperatures, but differs somewhat depending on R in the range $T \gtrsim 50$ K.

It is interesting to note that in spite of their reasonably high electrical conductivities (ranging from 100-1000 S cm^{-1}), the thermal conductivities of these nickelates, ranging from $1\,\text{Wm}^{-1}\text{K}^{-1}$ to $3\,\text{Wm}^{-1}\text{K}^{-1}$, is rather low, which, in turn, implies that the lattice thermal conductivity in these nickelates is intrinsically very low. This may be related to their complex layered structure. The low thermal conductivity and metal-like electrical conductivity above the MMT together indicates that the trilayer nickelates are potential oxide thermoelectric materials.

4. Magnetic susceptibility

The magnetic susceptibility (χ) is shown as Fig. 6. Our data shows good agreement with previous reports [27,35,36]. In $La_4Ni_3O_{10}$, χ exhibits a discernible kink at $T = 136$ K, which corresponds well with the MMT. In the temperature range $136\,\text{K} < T < 300\,\text{K}$, $\chi(T)$ decreases upon cooling which is uncharacteristic of a local moment system. However, at low temperatures it increases sharply. The upturn in χ could be fitted using the modified Curie-Weiss (CW) law: $\chi = \chi_o + C/(T - \theta_P)$ in the range $2\,\text{K} \leqslant \text{T} \leqslant 10\,\text{K}$, yielding $\chi_0 = 10^{-3}\,\text{emu mol}^{-1}\text{Oe}^{-1}$, the Curie constant $C = 1.7 \times 10^{-2}\,\text{emu mol}^{-1}\text{Oe}^{-1}\text{K}^{-1}$, and the paramagnetic Curie temperature $\theta_P \approx 2.7$ K. From a previous ARPES study [5], we know that a gap of $\approx$20 meV opens up in the $d_{3z^2-r^2}$ band below T_{MMT}, which may induce a localization of $d_{3z^2-r^2}$ electrons upon cooling, leading to the observed upturn below T_{MMT}. The overall magnetic behavior of $La_4Ni_3O_{10}$ exhibits a complex interplay of itinerant and local moment behavior.

The magnetic susceptibility of $Pr_4Ni_3O_{10}$ is dominated by the CW behavior associated with the Pr^{3+} moments. Additionally, a weak anomaly is also observed around $T \simeq 5$ K. The high-temperature χ could be fitted using the modified CW law, yielding $\chi_0 \approx 2.8 \times 10^{-3}\,\text{emu mol}^{-1}\text{Oe}^{-1}$, C $\approx$ $6.3\,\text{emu mol}^{-1}\text{Oe}^{-1}\text{K}^{-1}$, and $\theta_p \approx -36$ K in good agreement with literature [29]. The value of χ_0 is positive and comparable in magnitude to that for $La_4Ni_3O_{10}$. The negative sign of θ_p indicates the antiferromagnetic nature of exchange between the Pr^{3+} moments. The experimental effective magnetic

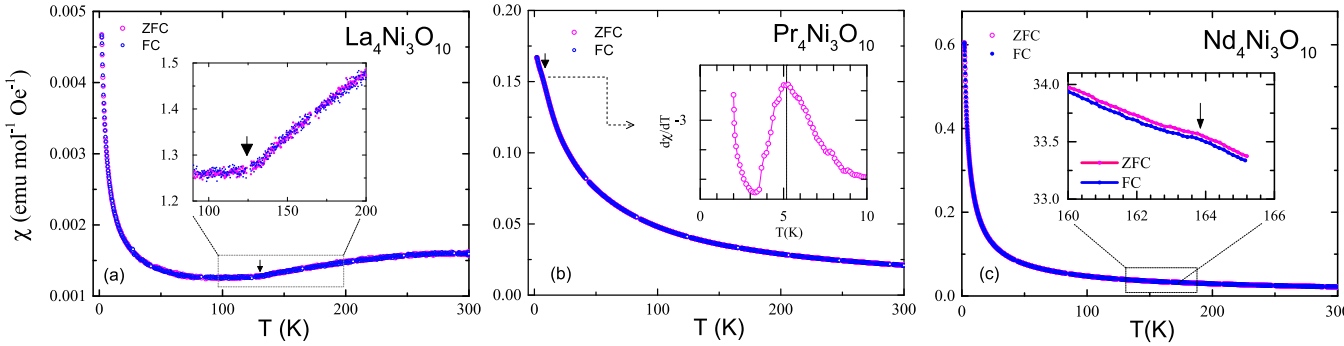

FIG. 6. Zero-field-cooled (ZFC) and field-cooled (FC) susceptibility (χ) of (a) $La_4Ni_3O_{10}$, (b) $Pr_4Ni_3O_{10}$, and (c) $Nd_4Ni_3O_{10}$ measured under an applied field of 5 kOe. The inset in: (a) shows a kink in susceptibility at T_{MMT}, in (b) the low-temperature anomaly is emphasized in the first derivative plot, in (c) the kink in susceptibility at T_{MMT}.

moment per formula unit can be estimated using the formula $\mu_{\text{eff}} = \sqrt{8C}$ which gives $\approx$7.2 μ_B. Theoretically, $\mu_{\text{eff}}/f.u.$ is given by $[4\mu^2_{\text{eff}}(\text{Pr}) + 3\mu^2_{\text{eff}}(\text{Ni})]^{\frac{1}{2}}$. Substituting the theoretical value of $\mu_{\text{eff}} = 3.58\ \mu_B$ per Pr^{3+} ion results in a relatively negligible moment on the Ni ions.

Though effective magnetic moments of Nd^{3+} and Pr^{3+} are nearly the same in free space, the low-temperature χ in $Nd_4Ni_3O_{10}$ is almost four times as large as that of $Pr_4Ni_3O_{10}$. This suggests the presence of strong crystal field effect that renders one-half of the Pr-moment effectively non-magnetic at low-temperature due to their singlet ground state as shown later in the paper. The CW fit in this case resulted in: $\chi_0 \sim 3.8 \times 10^{-3}$ emu mol^{-1}Oe^{-1}, $C \sim 6.3$ emu mol^{-1}Oe^{-1}K^{-1}, and $\theta_p = -46.5$ K. These values are in close agreement with those recently reported by Li *et al.* [13]. From C, the experimental μ_{eff} is estimated to be $\approx 7.1\mu_B/f.u.$, which is practically all due to the Nd^{3+}, suggesting that the local moment associated with Ni is comparatively negligible. The value of θ_p is high given the absence of any magnetic ordering, suggesting that a strong magnetic frustration is at play in these nickelates. For more information, we refer the reader to the Supplemental Material [19].

C. Specific heat

The specific heat (c_p) data of $R_4Ni_3O_{10}$ compounds exhibits a sharp anomaly at their respective MMTs, which is particularly pronounced for $Pr_4Ni_3O_{10}$ and $Nd_4Ni_3O_{10}$, which also show additional anomalies at low temperatures, associated with the rare-earth sublattice.

1. $La_4Ni_3O_{10}$

In $La_4Ni_3O_{10}$, the specific-heat anomaly occurs at 136 K as shown in Fig. 7. It should be emphasized that in a $La_4Ni_3O_{10}$ crystallizing in the *Bmab* space group, the specific-heat anomaly occurs at a temperature of $\approx$ 150 K as opposed to 136 K for the $P2_1/a$ phase [15]. This is consistent with our assessment of $P2_1/a$ as the majority phase in our samples. The applied magnetic field of 50 kOe (not shown) was found to have practically no effect on this anomaly. At low temperatures, c_p can be fitted using the equation $c_p = \gamma T + \beta T^3$, where γ and β represent the electronic and lattice contributions, respectively (see the lower inset in Fig. 7). The best-fit yields $\gamma \approx 15$ mJ mol^{-1}K^{-2}, $\beta \approx 0.43$ mJ mol K^{-4}. The Debye temperature (Θ_D) is calculated from β using the relation: $\beta = 12\pi^4 N k_B/5\Theta_D^3$, which gives a value of $\Theta_D \approx 450$ K. The values of Θ_D and γ obtained here are comparable to those previously reported [36]. From the value of γ, one can readily estimate the density of states at the Fermi energy, $D(E_F)$, using the expression $D(E_F) = 3\gamma/\pi^2 k_B^2$, which gives a value of $\approx 3.0 \times 10^{22}$ states eV^{-1} cm^{-3}. Now, using the carrier density n, one can estimate the corresponding density of states $D^\circ(E_F)$ at E_F using the free-electron model. Taking $n \approx 6.3 \times 10^{21}$ cm^{-3} [35], one gets $D^\circ(E_F) \approx 7.6 \times 10^{21}$ states eV^{-1} cm^{-3}. From the ratio $D(E_F)/D^\circ(E_F) = m^*/m_\circ$, we estimate the effective mass (m^*) for $La_4Ni_3O_{10}$ to be $m^* \approx 3.9m_\circ$, where $m_\circ$ is the bare electron mass, which is comparable to the value of m^* from the thermopower ($\approx 3.0m_\circ$). The small difference between the two can be due to the possible Fermi surface reconstruction below the MMT. Also, we have not accounted for the valley degeneracy, if any, which makes the effective mass derived from the density of states higher than the band effective mass by a factor of $N^{2/3}$, where N is the valley degeneracy. In any case, the important point is that from the value of m^* one can conclude that the electronic correlations in $La_4Ni_3O_{10}$ are only modestly enhanced.

2. $Pr_4Ni_3O_{10}$

Figure 7 shows the specific heat of $Pr_4Ni_3O_{10}$ where a sharp transition is observed at 156 K, which agrees nicely with the anomaly associated with the MMT in the transport data. In this case, too, the position and shape of the anomaly remains unaffected by the application of an external magnetic field. Apart from the expected peak at MMT, an additional broad anomaly is seen at low temperatures centered around $T_1 = 5$ K, which coincides with the anomaly in χ at the same temperature. Interestingly, the applied field up to 50 kOe has no significant effect on the shape or position of this anomaly, ruling out its Schottky-like origin.

To examine the contribution of $4f$ electrons associated with Pr to the specific heat (designated as c_{4f}^{Pr} in the following) at low temperatures, we subtracted the specific-heat data of $La_4Ni_3O_{10}$ from that of $Pr_4Ni_3O_{10}$. Since both are isostructural, with very similar molecular weights, it is, therefore, reasonable to approximate the lattice specific heat of $Pr_4Ni_3O_{10}$ with that of $La_4Ni_3O_{10}$. Furthermore, we assume that the small contribution due to Ni $3d$ electrons to the

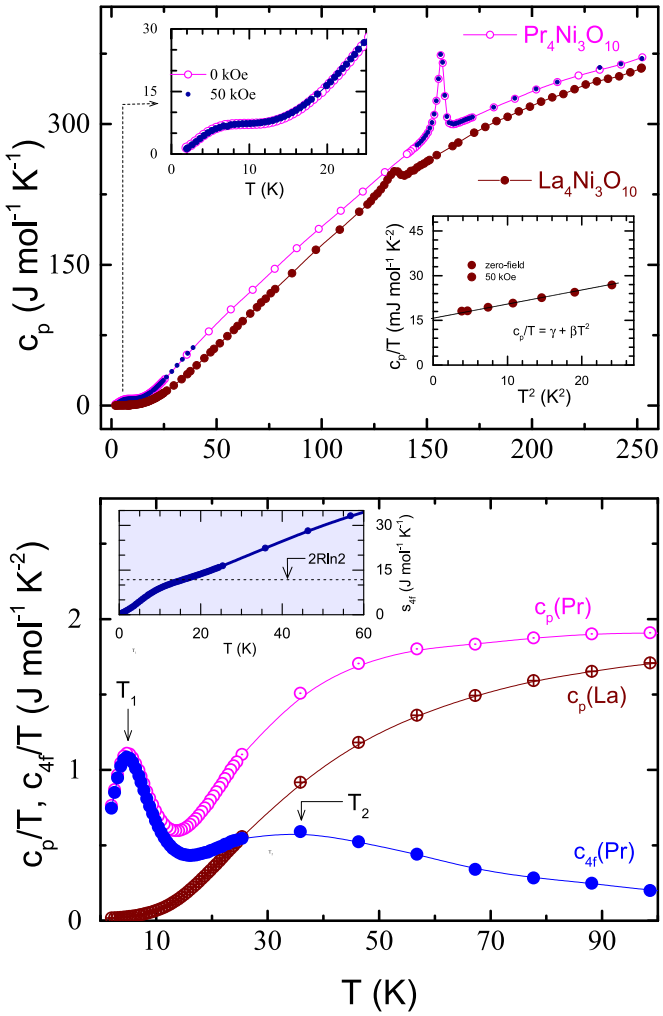

FIG. 7. (a) Temperature (T) variation of the specific heat (c_p) of $La_4Ni_3O_{10}$ and $Pr_4Ni_3O_{10}$. The upper inset in (a) highlights the presence of a broad anomaly in the low-temperature c_p of $Pr_4Ni_3O_{10}$ measured under zero-field and a field of 50 kOe. The immunity to magnetic field rules out the Schottky-like origin of this peak. The lower inset shows c_p/T vs T^2 of $La_4Ni_3O_{10}$ at low temperatures. The dashed line is a linear fit to the data. (b) $\frac{c_p}{T}$ against T. c_{4f}(Pr) represents the specific heat associated with the $4f$ electrons of Pr^{3+}, which is obtained by subtracting the specific heat of $La_4Ni_3O_{10}$ from that of $Pr_4Ni_3O_{10}$ (see text for details). Temperature variation of entropy associated with the $4f$ electrons of Pr^{3+} is shown as an inset.

specific heat does not vary much upon going from La to Pr, at least well below the MMT. This is a reasonable first approximation to make, given that T_{MMT} of the these nickelates is not very sensitive to the choice of R, in wide contrast with the members of the $RNiO_3$ series where the structural and physical properties are closed tied to the identity of the rare-earth ion [7].

c_{4f}^{Pr} obtained using this procedure is shown in Fig. 7(b) (lower panel) over the temperature range $2\,K \leqslant T \leqslant 100\,K$. Interestingly, beside the peak at $T_1 = 5\,K$, c_{4f}^{Pr} also exhibits an additional broad peak around $T_2 = 36\,K$. This new feature is likely a Schottky anomaly arising from the crystal-field splitting of the lowest $J = 4$ multiplet of the Pr^{3+} ions. To understand this further, we estimate the magnetic entropy (s_{4f}) buried under the peak at T_1 using the formula: $s_{4f} = \int_0^T (c_{4f}^{Pr}/T')dT'$. For our rough estimate, we extrapolate c_{4f}^{Pr} below $T = 2\,K$ linearly to $T = 0\,K$. The calculated s_{4f} is shown as an inset in the lower panel of Fig. 7. It shows a relatively steep rise up to 10 K, but continues to increase, albeit at a slower rate, upon heating beyond 15 K. The region between 10 K and 15 K is where the crossover from higher ($T <$ 10 K) to slower ($T >$ 15 K) rates happens. The magnetic entropy released in the temperature range $T \leqslant 15\,K$ ($\approx 3T_1$) is $\approx 11.5\,J\,mol^{-1}K^{-1}$, i.e., $\approx 2.9\,J\,Pr - mol^{-1}K^{-1}$, which is approximately $\frac{1}{2}$ of $R\ln 2$. What this suggests is that the peak at T_1 is likely due to the magnetic ordering of $\frac{1}{2}$ of the Pr^{3+} ions per $Pr_4Ni_3O_{10}$ formula unit, which is plausible since there are two types of Pr coordinations in this structure: ninefold (RS layers) and 12-fold (PB layers). Incidentally, Pr^{3+} in the perovskite $PrNiO_3$ has a nonmagnetic singlet ground state [37]. Since the coordination of Pr^{3+} ions in the PB layers of $Pr_4Ni_3O_{10}$ is analogous to that in $PrNiO_3$, it is reasonable to assume that they, too, have a singlet ground state with no magnetic ordering. Therefore, we can tentatively associate the peak at T_1 to the magnetic ordering of the ninefold coordinated Pr^{3+} ions. The increase in s_{4f} beyond 15 K can be attributed to the higher lying crystal-field levels as discussed further. A similar scenario has been previously reported for the compound Pr_3RuO_7, which has two types of Pr coordinations, namely, eightfold and sevenfold, with Pr ions in the sevenfold coordination having a crystal-field split singlet ground state, and those in the eightfold coordination a doublet [38].

However, the question arises as to why the peak associated with the magnetic ordering of Pr^{3+} ions in the RS layer is not as sharp as is typically seen at a long-range-ordered magnetic transitions. To answer this question, one should see that for the ninefold coordinated Pr^{3+} ions, there are, in fact, two distinct crystallographically sites (Pr1 and Pr2) as discussed in Sec. III A. Due to minor differences in bond angles and bond lengths around Pr1 and Pr2, the exchange integrals J_{11} (within the Pr1 sublattice), J_{22} (within the Pr2 sublattice), and intersite J_{12} may differ slightly, which could be one of the reasons for the c_p anomaly at T_1, associated with ordering of Pr1 and Pr2, to be broad. The other reason could be related to the fact that a Pr^{3+} moment in a RS layer is only weakly coupled to the Pr^{3+} moments in the RS layer above it (see Fig. 1), leading to a quasi-two-dimensional behavior.

Let us now turn our attention to the peak at T_2 which seems to arise due to the crystal-field splitting of the lowest J-multiplet of Pr^{3+} ions. In a previous inelastic neutron scattering study on the perovskite compound $PrNiO_3$ [37], it was found that the ninefold degenerate J multiplet of the Pr^{3+} ion splits into nine singlets due to the crystal-field effect. The energy difference between the ground-state singlet (E_0^1) and the first excited state (E_1^1) is 6.4 meV or approximately 70 K. In the first-order approximation, the crystal-field splitting of Pr ions in the PB layers of $Pr_4Ni_3O_{10}$ can be assumed to be similar to that in the compound $PrNiO_3$. Within this assumption, the Schottky anomaly due to the ground and first excited singlet is expected to be centered slightly below $T = (E_1^1 - E_0^1)/2k_B \approx 35$ K, which is remarkably close to the position of the peak at T_2. Since the second excited singlet for Pr in the PB layers is located around $E_2^1 = 15$ meV (≈ 165 K),

it is too high up to have any significant effect on the Schottky anomaly arising due to the (E_0^1, E_1^1) pair.

It can therefore be concluded that the Pr ions in the PB layer have a singlet ground state due to a crystal-field effect, with a broad Schottky anomaly associated with the ground and first excited singlet pair. On the other hand, Pr ions in the RS layers have a crystal-field split doublet as their ground state, and undergo magnetic ordering around T_1. The observed increase in s_{4f} above $2\,T_1$ is partly due to E_0^1-E_1^1 excitations associated with Pr ions in the PB layer, and partly due to the higher lying crystal-field-split levels of Pr ions in the RS layers. In the absence of a detailed crystal-field splitting scheme for the Pr ions in the RS layers, a quantitative analysis of the low-temperature specific heat is left as a future exercise.

3. $Nd_4Ni_3O_{10}$

Figure 8(a) shows the specific heat of $Nd_4Ni_3O_{10}$, which is characterized by a sharp anomaly at $T = 160$ K. The position of this anomaly is in fairly good agreement with the MMT inferred from the transport data, and is found to be independent of an applied magnetic field at least up to 50 kOe. The low temperature c_p is characterized by an upturn below $T = 10$ K. Under an applied magnetic field, this upturn evolves, leading to a broad peak, centered around 4 K under $H = 50$ kOe, which progressively shifts to higher temperatures with increasing magnetic field. This behavior is reminiscent of a Schottky-like anomaly, which often arises in the rare-earth-based compounds due to the crystal-field splitting.

To investigate this further, we estimate the specific heat associated with $4f$ electrons of Nd, labeled c_{4f}^{Nd}. The specific heat of $La_4Ni_3O_{10}$ is used as a lattice template and also to subtract the small magnetic specific heat associated with the Ni sublattice. c_{4f}^{Nd} obtained in this manner is displayed in the lower panel of Fig. 8 (inset). At $T = 2$ K, it has a value of about $\sim 6.9\,\mathrm{J\,mol^{-1}K^{-1}}$, which decreases sharply upon heating but remains substantial ($\sim 3.5\,\mathrm{J\,mol^{-1}K^{-1}}$) even at $T = 12$ K, and increases again upon further heating, exhibiting a broad Schottky-like anomaly near $T = 50$ K that can be attributed to the higher-lying crystal-field split levels of Nd^{3+} ions. In $NdNiO_3$, for example, the lowest $^4I_{9/2}$ multiplet of Nd^{3+} ion splits into *five* Kramers doublets with the first excited doublet situated around 100 K above the ground doublet [39]. Since Nd^{3+} ions in the PB layers of $Nd_4Ni_3O_{10}$ are analogously coordinated, one can assume a similar crystal field splitting scheme for them. On the other hand, for the ninefold coordinated Nd^{3+} ions, the splitting scheme may be different. However, since Nd^{3+} is a Kramers ion with three electrons in the f orbitals, in the absence of a magnetic field each crystal-field-split level should at least be twofold degenerate: i.e., for the ninefold coordinated Nd^{3+} ions, the ground and first excited state crystal-field-split levels can have degeneracies as follows: $g_0 = 2$, $g_1 = 2$, $g_0 = 2$, $g_1 = 4$, or $g_0 = 4$, $g_1 = 2$. Thus, the ratio $\frac{g_1}{g_0}$, which appears in the expression for the Schottky anomaly, can take values 1, 2, or 0.5, respectively. Note that for Nd^{3+} ions in the PB layer, this ratio will be 1. With this as an input, one can try fitting the broad peak in c_{4f}

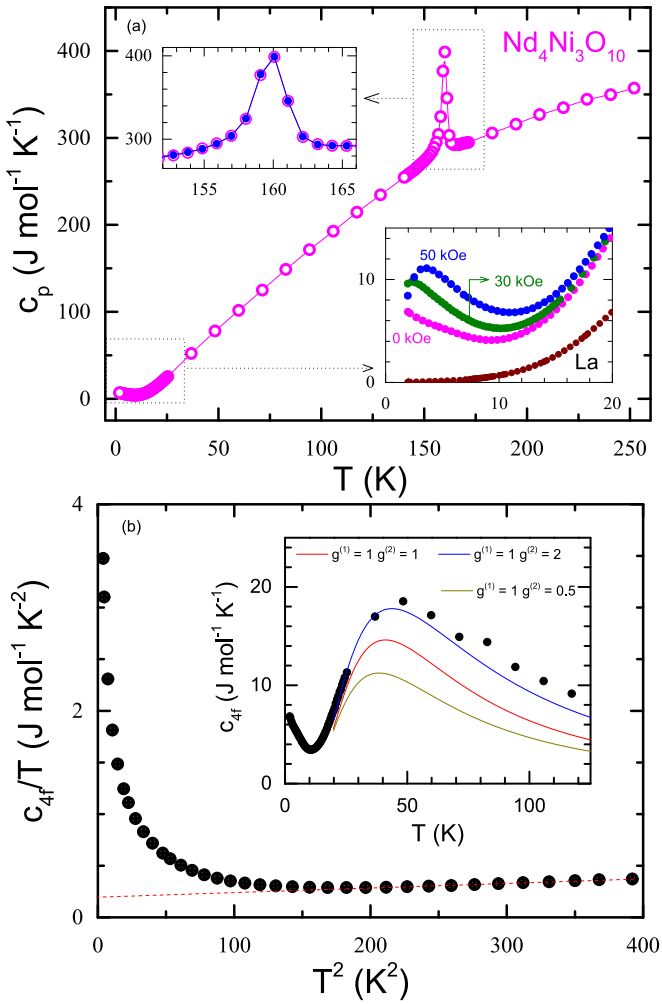

FIG. 8. (a) Specific heat (c_p) of $Nd_4Ni_3O_{10}$. Lower inset shows c_p in the low-temperature range for an applied field of 0 kOe, 30 kOe, and 50 kOe; c_p of $La_4Ni_3O_{10}$ is also shown for comparison. Upper inset shows an expanded view of the anomaly at MMT under zero field and a field of 50 kOe. (b) Low-temperature specific heat associated with the $4f$ electrons of $Nd_4Ni_3O_{10}$ is plotted as c_{4f}/T versus T^2; inset shows c_{4f} versus T up to $T = 120$ K to show the presence of a pronounced Schottky anomaly near $T = 40$ K. The modified Schottky fittings for three cases: $g^{(1)} = 1$, $g^{(2)} = 1$ (red), $g^{(1)} = 1$, $g^{(2)} = 2$ (blue), and $g^{(1)} = 1$, $g^{(2)} = 0.5$ (khaki) (see text for details)

near 40 K using the expression $c_{\mathrm{Sch}} = c_{\mathrm{Sch}}^{(1)} + c_{\mathrm{Sch}}^{(2)}$, where

$$c_{\mathrm{Sch}}^{(i)} = 2R\left(\frac{\Delta_i}{T}\right)^2 \frac{g^{(i)}\exp\left(\frac{-\Delta_i}{T}\right)}{\left[1 + g^{(i)}\exp\left(\frac{-\Delta_i}{T}\right)\right]^2}. \tag{3}$$

In this expression, R is the universal gas constant, Δ is the splitting between the ground and first excited state, and g is the ratio $\frac{g_1}{g_0}$. Here, the index i is used for the the two types of coordinations, viz., $i = 1$ corresponding to the 12-fold coordination, and $i = 2$ corresponding to the ninefold. The prefactor 2 accounts for the number of Nd^{3+} ions per formula unit in each type of layers. The fitting result for $g^{(1)} = 1$, $g^{(2)} = 1$ (fit1), $g^{(1)} = 1$, $g^{(2)} = 2$ (fit2), and $g^{(1)} = 1$, $g^{(2)} = 0.5$ (fit3) are shown in the inset of Fig. 8(b). The corresponding values of Δ_1 and Δ_2 for these fits are 98 K and 98 K for (fit1), 150 K and 95 K for (fit2), and 87 K and

93 K for (fit3), respectively. Clearly, the best fit corresponds to (fit2), which implies that the ground state of Nd^{3+} ions in the ninefold coordination is also a Kramers doublet, with a quartet for the first excited state.

Let us now turn our attention to the increase in c_{4f}^{Nd} upon cooling below $T = 10$ K. In $NdNiO_3$, a similar upturn leading to a broad peak around $T = 1.7$ K had been previously reported [39]. It was argued to arise from the exchange splitting of the ground-state doublet. However, unlike $NdNiO_3$, in $Nd_4Ni_3O_{10}$ the Ni moments are not ordered and hence the Ni–Nd exchange field in this case is almost nonexistent. On the other hand, it might be that this upturn is precursory to an impending magnetic ordering of the Nd moments at further low temperatures. After all, the Nd-Nd exchange, as inferred from the high-temperature CW fit, is about −40 K, which is rather high. This could then be a case closely analogous to the case of Nd_2O_3 recently reported, which also exhibits a high $\theta_p \simeq -24$ K, but with long-range order setting in only below $T = 0.55$ K. Surprisingly, c_p of Nd_2O_3 shows not only a sharp peak at 0.55 K, corresponding to the long-range ordering of Nd moments, but also a broad feature centered around 1.5 K. The authors report that the entropy associated with this broad peak must be taken into account to recover the $R \ln 2$ entropy expected from a ground-state doublet, suggesting a complex two-step ordering of the Nd moments in Nd_2O_3. The c_p of $Nd_4Ni_3O_{10}$ also shows a broad peak at $T \approx 1.8$ K [13], which suggests that a phenomenology analogous to Nd_2O_3 might also be at play here. Further studies down to much lower temperatures would be interesting to explore this analogy further and to understand the true ground state of the Nd sublattice.

Finally, c_{4f}^{Nd}/T versus T^2 is plotted in the lower panel of Fig. 8. The data from 12 K to 20 K can be fitted to a straight line whose intercept on the $y-$axis is $\sim$150 mJ mol^{-1}K^{-2}. Indeed, in Ref. [13], a high γ value of 146 mJ mol^{-1}K^{-2} is reported by fitting c_p/T versus T^2 to $\gamma + \beta T^2$ in this temperature range. However, caution must be exercised while interpreting the intercept value in this case since c_p in this temperature range, as shown in the inset of Fig. 8(b), is overwhelmed by the Schottky contribution arising from the crystal-field-split lowest $J-$multiplet of Nd^{3+} ions. It is for this reason we believe that the erroneously high γ value in Ref. [13] misled the authors to conclude a "novel" heavy-electron behavior in $Nd_4Ni_3O_{10}$. In fact, as shown in the Supplemental Material [19], if one uses the same procedure for $Pr_4Ni_3O_{10}$, a high γ value of $\approx$300 mJ mol^{-1}K^{-2} will emerge, but we know from the work of Huangfu *et al.* [16] that the resistivity of a $Pr_4Ni_3O_{10}$ single crystal decreases upon cooling at low temperatures, i.e., no heavy-electron behavior is observed in the transport studies. In fact, as is well documented in the heavy-fermion literature, if the electronic specific heat γ in such cases is derived by extrapolating the high-temperature specific heat data to $T = 0$ K using $\gamma T + \beta T^3$, unusually large values of γ emerge, which can be *falsely* interpreted as arising due to the heavy fermion behavior.

D. Thermal expansion and Grüneisen analysis

The temperature dependence of length changes studied by capacitive dilatometry, shown in Fig. 9, follows the volume dependence as measured using the x-ray diffraction data [see Figs. 2(f1)–2(f3)]. However, while there is quantitative agreement for $Pr_4Ni_3O_{10}$, discrepancies are noted for $La_4Ni_3O_{10}$ and $Nd_4Ni_3O_{10}$. Specifically, the dilatometric length changes are about 25% and 45% larger than suggested by x-ray diffraction, respectively. The data are isotropic, i.e., we find the behavior to be the same when measuring along different directions of the polycrystalline cuboids, which excludes a simple nonrandom orientation effect to cause this discrepancy.

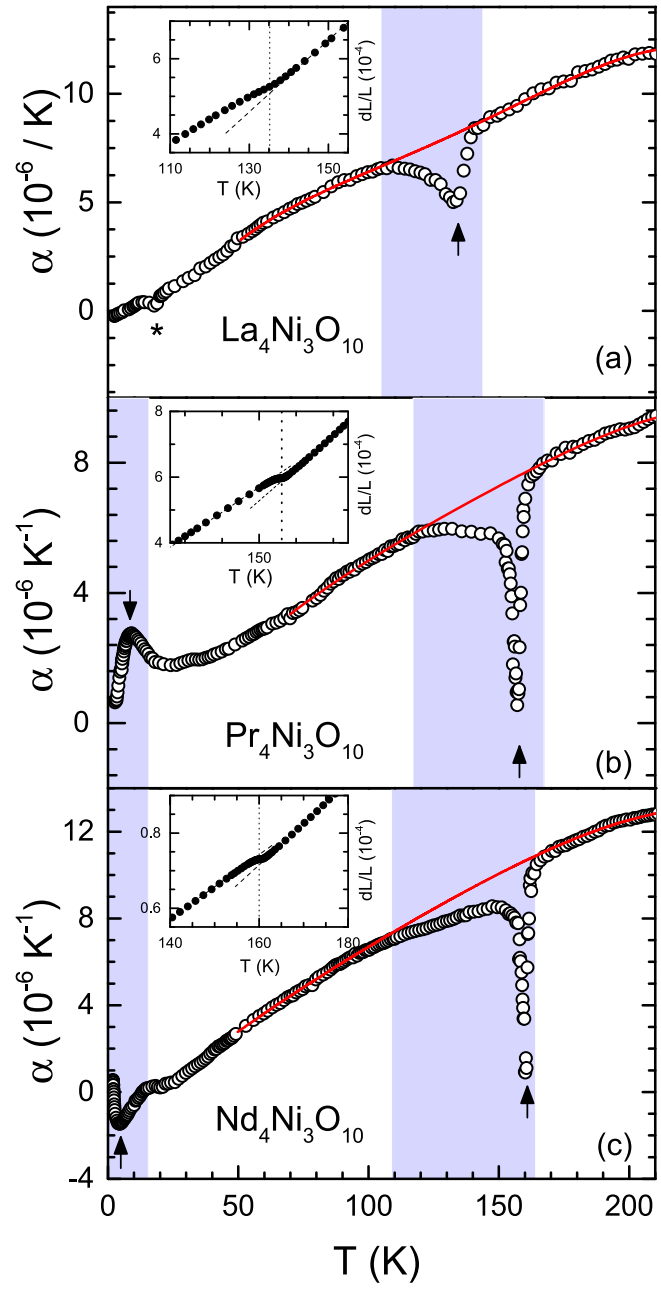

FIG. 9. Temperature dependence of the thermal expansion coefficient α of $La_4Ni_3O_{10}$, $Pr_4Ni_3O_{10}$, and $Nd_4Ni_3O_{10}$. The red line shows a polynomial estimate of the background (see text for details). The arrows mark the position of T_{MMT}. The asterisk in the upper panel indicates an experimental artifact. The additional low-temperature peak in $Pr_4Ni_3O_{10}$ and $Nd_4Ni_3O_{10}$ is likely due to the crystal-field excitations. The inset shows length change (dL/L) around T_{MMT}; the dotted line is a guide to the eye.

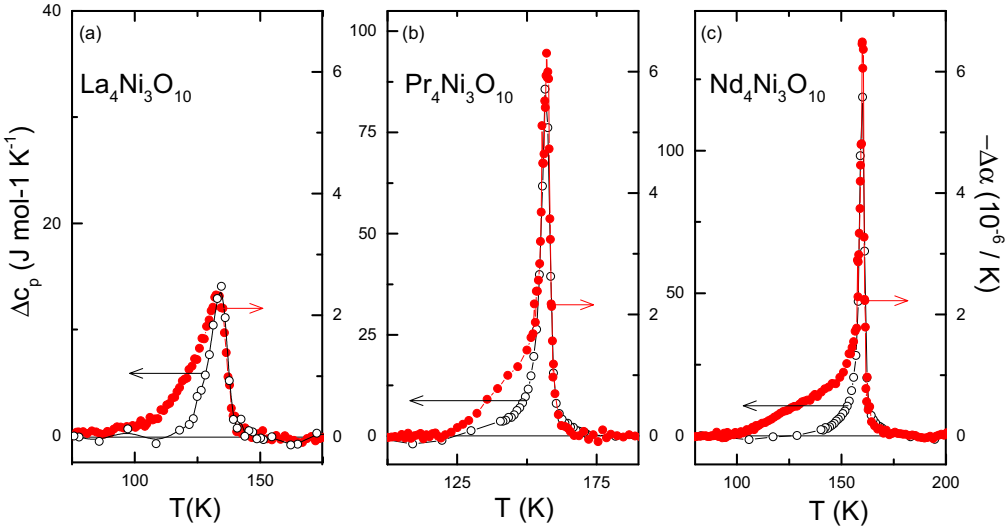

FIG. 10. Anomalies in the specific heat and the negative thermal expansion coefficient of $R_4Ni_3O_{10}$ with R = La, Pr, and Nd. The anomaly size in (a) and (c) has been rescaled according to the x-ray diffraction results (see the text). Note the same scale of the thermal expansion ordinate in all graphs.

Instead, the data suggest a nonuniform internal stress distribution within the polycrystalline samples which can lead, in porous materials, to larger thermal expansion than in the bulk [40].

The length changes in $R_4Ni_3O_{10}$ evidence significant coupling of electronic and structural degrees of freedom. Specifically, there are pronounced anomalies at T_{MMT} in all studied materials. In $La_4Ni_3O_{10}$, the data in Fig. 9 displays a broad feature which signals shrinking of the sample volume upon exiting the MMT phase while heating the sample. Qualitatively, this implies negative hydrostatic pressure dependence $dT_{MMT}/dp < 0$. The minimum of the thermal expansion anomaly appears at $T_{MMT} = 134$ K, suggesting either a weak first-order character of the transition or a somehow truncated λ-like behavior similar to what is indicated by the specific heat anomaly (cf. Fig. 7).

To estimate the background contribution to the thermal expansion coefficient, a polynomial was fitted to the data well below and above the thermal expansion anomaly as shown in Fig. 9 [41]. The background α^{bgr} mainly reflects the phonon contribution. Due to the large size of the anomaly, using different temperature ranges for the determination of the background and/or choosing different fit functions does not change the result significantly. Subtracting α^{bgr} from the data yields the anomaly contribution to the thermal expansion coefficient $\Delta\alpha$ as shown in Fig. 10(a). Recalling the discrepancy of dilatometric and XRD length changes mentioned above for $La_4Ni_3O_{10}$ and $Nd_4Ni_3O_{10}$, for the following quantitative analysis of both we have scaled the dilatometric data to the XRD results. Quantitatively, our analysis then yields total anomalous length changes $\Delta_t L/L = \int \Delta\alpha dT = -4.2(9) \times 10^{-5}$.

When replacing La by Pr and Nd in $R_4Ni_3O_{10}$, the anomalies in the thermal expansion at T_{MMT} become significantly sharper and evidence rather discontinuous behavior (see Fig. 9). In addition, there are pronounced features at low temperatures (marked by arrows) that are associated with the rare-earth sublattice. In particular, the data clearly confirm negative volume expansion in $Nd_4Ni_3O_{10}$ below ∼20 K. At higher temperatures, the sharp anomalies at 156 K (R = Pr) and 160 K (R = Nd) at T_{MMT} are accompanied by a regime of rather continuous length changes which extends from T_{MMT} down to about 110 K, i.e., it is significantly larger than the anomaly regime in $La_4Ni_3O_{10}$. Applying the procedure described above for determining the background yields the thermal expansion anomalies as displayed in Figs 10(b) and 10(c) for the two compounds.

The anomalies $\Delta\alpha$ in the thermal expansion coefficients at T_{MMT} are presented in Fig. 10 together with the respective anomalies of the specific heat. The latter have been derived by estimating the background specific heat analogously to the procedure used for the thermal expansion data and by using the same fitting regimes in both cases [41]. For each composition, scaling of Δc_p and $\Delta\alpha$ has been chosen to obtain the best overlap of the specific heat and thermal expansion data around T_{MMT} and above. The fact that the thermal expansion and specific-heat anomalies are proportional at T_{MMT} implies a T-independent Grüneisen parameter describing the ratio of pressure and temperature dependence of entropy changes in this temperature range. This observation implies the presence of a single dominant energy scale ϵ [42]. In contrast, the fact that Grüneisen scaling starts to fail at around 10 K below T_{MMT} indicates the presence of more than one relevant degree of freedom. In the temperature regime around T_{MMT} and above, the corresponding scaling parameter is the Grüneisen parameter [43]:

$$\Gamma = \frac{3\Delta\alpha}{\Delta c_p} = \frac{1}{V}\frac{\partial \ln \epsilon}{\partial p}\bigg|_T. \tag{4}$$

Our analysis yields the Γ values summarized in Table II. Using the Ehrenfest relation, the obtained values of Γ yield the hydrostatic pressure dependencies of the ordering temperature at vanishing pressure, i.e., $dT_{MMT}/dp = T_{MMT}V_m\Gamma$. The results deduced using the molar volume V_m are shown in Table II.

TABLE II. Total anomalous length and entropy changes $\Delta_t L/L = \int \Delta\alpha dT$ and $\Delta_t S = \int \Delta c_p^{\mathrm{MMT}}/T dT$, discontinuous length changes $\Delta_d L/L$, Grüneisen parameter Γ, and hydrostatic pressure dependence of T_{MMT} of $R_4Ni_3O_{10}$ (see the text).

	$\Delta_t L/L$	$\Delta_d L/L$	$\Delta_t S$	Γ	dT_{MMT}/dp
$La_4Ni_3O_{10}$	$-4(1)\times10^{-5}$	–	1.0(3) J/(mol K)	$-4.9(9)\times10^{-7}$ mol/J	−8(2) K/GPa
$Pr_4Ni_3O_{10}$	$-5(1)\times10^{-5}$	$-3.1(6)\times10^{-5}$	3.1(6) J/(mol K)	$-2.3(6)\times10^{-7}$ mol/J	−4(1) K/GPa
$Nd_4Ni_3O_{10}$	$-5.1(4)\times10^{-5}$	$-2.6(2)\times10^{-5}$	3.5(9) J/(mol K)	$-1.4(4)\times10^{-7}$ mol/J	−3(1) K/GPa

The obtained initial slopes of hydrostatic pressure dependencies of T_{MMT} are comparable to values reported from measurements of the electrical resistivity under pressure. Specifically, Wu *et al.* report −6.9 K/GPa for $La_4Ni_3O_{10}$, which nicely agrees with the results of the Grüneisen analysis presented above. The comparison with $Nd_4Ni_3O_{10}$ studied in Ref. [13] is, however, ambiguous. On the one hand, Li *et al.* [13] report discontinuous shrinking of the unit cell volume at T_{MMT} by 0.08% while cooling, which, both, qualitatively and quantitatively, contrasts our data [cf. inset of Fig. 9(c)]. In particular, this value implies a *positive* hydrostatic pressure dependence of about +35 K/GPa [44]. However, at the same time, an initial *negative* hydrostatic pressure dependence of about −8 K/GPa is reported in Ref. [13] which thermodynamically contradicts the reported volume changes at T_{MMT} but is reasonably consistent with the results of our Grüneisen analysis.

The broad region of anomalous length changes between T_{MMT} and ∼100 K signals a clear temperature variation of the Grüneisen ratio in this temperature regime, the reason of which is not fully clear. In general, the fact that capacitance dilatometry is obtained under small but finite pressure, which in the case at hand is estimated to about 0.6(1) MPa, may affect measurements, in particular, on polycrystalline samples. The fact that the dilatometer detects volume increase, however, renders a scenario as observed in recent studies of electronic nematicity of LaFeAsO rather unlikely, where the shear modulus C_{66} is the elastic soft mode of the associated nematic transition so dilatometry under finite pressure results in associated volume decrease [45,46]. We also exclude that variation of Γ is associated with incompletely resolved strain from the discontinuous transition at T_{MMT} because the measurements have been performed upon heating and the temperature regime of the observed anomaly is very large. Instead, we conclude the presence of a competing ordering phenomenon as suggested by the failure of Grüneisen scaling [42]. Intriguingly, a temperature regime of unexpected behavior has also been detected in the out-of-plane resistivity $\rho_\perp$ in $Pr_4Ni_3O_{10}$ single crystals where, in contrast to the in-plane resistivity, an increase of $\rho_\perp$ upon cooling, i.e., insulating behavior, is observed in a large temperature regime [14]. It is tempting to trace back this intermediate temperature regime of $d\rho_\perp/dT < 0$, i.e., a metal-to-insulator-like behavior of $\rho_\perp$ at T_{MMT}, to the competing degree of freedom which manifests in the thermal expansion coefficient and change of Grüneisen parameter shown in Fig. 10(b).

IV. SUMMARY AND CONCLUSIONS

We investigated the trilayer nickelates $R_4Ni_3O_{10}$ (R = La, Pr, and Nd) that are $n = 3$ members of the RP series. We focused our investigations on understanding the following important aspects concerning the properties of these compounds: (i) What is the correct space group characterizing the room-temperature crystal structure of these compounds? (ii) Is there a structural phase transition at T_{MMT}? (iii) How do various thermodynamic quantities, including resistivity, magnetic susceptibility, specific heat, thermopower, thermal conductivity, and thermal expansion coefficient vary across MMT? and (iv) to understand the magnetic behavior of the rare-earth sublattices in $Pr_4Ni_3O_{10}$ and $Nd_4Ni_3O_{10}$.

To address these questions, we synthesized high-quality samples using the sol-gel method. These samples were then subject to a high-resolution synchrotron powder x-ray diffraction at the ALBA synchrotron source, both at 300 K and lower temperatures down to 90 K. A thorough analysis confirms that these compounds crystallize in the monoclinic $P2_1/a, Z = 4$ phase. Absence of new peaks emerging, or splitting of the existing peaks ruled out any lowering of the lattice symmetry accompanying this transition. The thermal expansion coefficient also captured the anomaly at T_{MMT} rather vividly. From the analysis of $\Delta\alpha$, we conclude that the MMT anomaly becomes more first-order-like as we go to smaller lanthanide ionic radii (and thereby larger distortions from the perovskite structure). This was further corroborated by temperature variation of various physical properties.

Resistivity data of all samples exhibit sharp jump or discontinuity at their respective T_{MMT} and an upturn, i.e., with $d\rho/dT < 0$, at low temperatures. We show that this upturn is likely a consequence of weak-localization arising due to inelastic electron-electron interactions. This result is in agreement with Ref. [27], where resistivity of $La_4Ni_3O_{10}$ has been analyzed in considerable detail. In particular, we excluded a Kondo-like mechanism in the Ni sublattice, leading to $d\rho/dT < 0$ as has been proposed recently [13]. This result is further strengthened by thermopower and specific-heat experiments. From thermopower and specific heat, we found the effective mass of the charge carriers to range around $3m_\circ$, which indicates that the electronic correlations are at best moderately enhanced.

The magnetic ground state of the R ions in $Pr_4Ni_3O_{10}$ and $Nd_4Ni_3O_{10}$ is shown to be rather interesting. First, the CW temperature (θ_p) for both these compounds is of the order of −40 K; however, the long-range ordering remains suppressed down to temperatures as low as 5 K for $Pr_4Ni_3O_{10}$ and less than 2 K for $Nd_4Ni_3O_{10}$, suggesting the presence of strong magnetic frustration, which may be related to their layered structure that renders the R^{3+} moments located in the RS layers quasi-two-dimensional. From the analysis of c_p and χ, we infer that in $Pr_4Ni_3O_{10}$, the Pr^{3+} ions located in the PB layers exhibit a crystal-field-split nonmagnetic singlet ground state, while those located in the RS layers show a ground

state doublet with an antiferromagnetic ordering below about 5 K.

In $Nd_4Ni_3O_{10}$, on the other hand, all four Nd ions in the formula unit exhibit a Kramers doublet ground state with first excited state as doublet for one-half of the Nd ions and quartet for the remaining half, giving rise to a pronounced Schottky-type anomaly centered around $T = 35$ K. The low-temperature specific heat of both $Pr_4Ni_3O_{10}$ and $Nd_4Ni_3O_{10}$ is found to be overwhelmed by the Schottky-like contributions arising from the crystal-field excitations associated with the lowest J multiplet of the rare-earth ions, which tends to *falsely* inflate the value of γ.

In summary, the rare-earth sublattice in $R_4Ni_3O_{10}$ compounds with $R =$ Pr and Nd exhibit very intriguing behavior which should be subject to further examination down to much lower temperatures. Due to the possibility of single-crystal growth of higher-order RP members under oxygen pressure using the floating-zone method, the interesting low-temperature behavior of these compounds as revealed here should attract significant further interest.

ACKNOWLEDGMENTS

We are thankful to beamline scientists Francois Fauth, Catalin Popescu, and Aleksandr Missiul at the MSPD-BL04 beamline at ALBA Synchrotron facility. S.S., D.R., and S.R.M. would like to acknowledge the Department of Science and Technology, India (Grant No. SR/NM/Z-07/2015) for providing financial support for carrying out the Synchrotron experiments at ALBA, and to the Jawaharlal Nehru Centre for Advanced Scientific Research (JNCASR) for facilitating it. S.S. acknowledges financial support form SERB (Grant No. WMR/2016/003792). R.K., M.H., and S.Spachmann acknowledges support by Deutsche Forschungsgemeinschaft (DFG) through Grant No. KL 1824/13-1 and by BMBF via SpinFun (Grant No. 13XP5088).

[1] G. Giovannetti, S. Kumar, D. Khomskii, S. Picozzi, and J. van den Brink, Phys. Rev. Lett. **103**, 156401 (2009).
[2] H. J. Zhao, W. Ren, Y. Yang, J. Íñiguez, X. M. Chen, and L. Bellaiche, Nat. Commun. **5**, 4021 (2014).
[3] M. Hepting, M. Minola, A. Frano, G. Cristiani, G. Logvenov, E. Schierle, M. Wu, M. Bluschke, E. Weschke, H.-U. Habermeier *et al.*, Phys. Rev. Lett. **113**, 227206 (2014).
[4] D. Li, K. Lee, B. Y. Wang, M. Osada, S. Crossley, H. R. Lee, Y. Cui, Y. Hikita, and H. Y. Hwang, Nat. Lett. **572**, 624 (2019).
[5] H. Li, X. Zhou, T. Nummy, J. Zhang, V. Pardo, W. E. Pickett, J. F. Mitchell, and D. S. Dessau, Nat. Commun. **8**, 704 (2017).
[6] J. Zhang, A. S. Botana, J. W. Freeland, D. Phelan, H. Zheng, V. Pardo, M. R. Norman, and J. F. Mitchell, Nat. Phys. **13**, 864 (2017).
[7] S. Catalano, M. Gibert, J. Fowlie, J. Íñiguez, J.-M. Triscone, and J. Kreisel, Rep. Prog. Phys. **81**, 046501 (2018).
[8] Note, an exception to this being $La_2NiO_{4-\delta}$ ($n = 1$), which shows an interesting phase diagram as a function of its oxygen off-stoichiometry δ (see, for example, Ref. [9]).
[9] M. Greenblatt, Curr. Opin. Solid State Mater. Sci. **2**, 174 (1997).
[10] J. M. D. Coey, M. Viret, and S. von Molnár, Adv. Phys. **48**, 167 (1999).
[11] J. Zhang, D. Phelan, A. S. Botana, Y.-S. Chen, H. Zheng, M. Krogstad, S. G. Wang, Y. Qiu, J. A. Rodriguez-Rivera, R. Osborn *et al.*, arXiv:2004.07897 (2020).
[12] D. Puggioni and J. M. Rondinelli, Phys. Rev. B **97**, 115116 (2018).
[13] B.-Z. Li, C. Wang, P. T. Yang, J. P. Sun, Y.-B. Liu, J. Wu, Z. Ren, J.-G. Cheng, G.-M. Zhang, and G.-H. Cao, Phys. Rev. B **101**, 195142 (2020).
[14] S. Huangfu, G. D. Jakub, X. Zhang, O. Blacque, P. Puphal, E. Pomjakushina, F. O. von Rohr, and A. Schilling, Phys. Rev. B **101**, 104104 (2020).
[15] J. Zhang, H. Zheng, Y.-S. Chen, Y. Ren, M. Yonemura, A. Huq, and J. F. Mitchell, Phys. Rev. Mater. **4**, 083402 (2020).
[16] S. Huangfu, X. Zhang, and A. Schilling, Phys. Rev. Research **2**, 033247 (2020).
[17] M. Deus Carvalho, F. Madalena A. Costa, I. da Silva Pereira, A. Wattiaux, J. Marc Bassat, J. Claude Grenier, and M. Pouchard, J. Mater. Chem. **7**, 2107 (1997).
[18] Z. Zhang, M. Greenblatt, and J. Goodenough, J. Solid State Chem. **108**, 402 (1994).
[19] See Supplemental Material at https://link.aps.org/supplemental/10.1103/PhysRevB.102.195144 for sample synthesis method, structure refinement using various space groups, select R–O and Ni–O bond distances, TGA, low-temperature x-ray diffraction, isothermal magnetization, and specific heat data.
[20] F. Fauth, R. Boer, F. Gil-Ortiz, C. Popescu, O. Vallcorba, I. Peral, D. Fullà, J. Benach, and J. Juanhuix, Eur. Phys. J. Plus **130**, 160 (2015).
[21] J. Rodríguez-Carvajal, Physica B **192**, 55 (1993).
[22] R. Küchler, T. Bauer, M. Brando, and F. Steglich, Rev. Sci. Instrum. **83**, 095102 (2012).
[23] M. Seppänen, J. Metallugy **8**, 191 (1979).
[24] A. K. Tkalich, V. P. Glaskov, V. A. Somenkov, S. Shil'shtein, A. E. Kar'kin, and A. V. Mirmel'shtein, Superconductivity **4**, 2280 (1991).
[25] V. Voronin, I. Berger, V. Cherepanov, L. Gavrilova, A. Petrov, A. Ancharov, B. Tolochko, and S. Nikitenko, Nucl. Instrum. Methods **470**, 202 (2001), Proceedings of the 13th National Synchrotron Radiation Conference.
[26] C. D. Ling, D. N. Argyriou, G. Wu, and J. Neumeier, J. Solid State Chem. **152**, 517 (2000).
[27] S. Kumar, Ø. Fjellvåg, A. O. Sjåstad, and H. Fjellvåg, J. Magn. Magn. Mater. **496**, 165915 (2020).
[28] M. U. Nagell, W. A. Sławiński, P. Vajeeston, H. Fjellvåg, and A. O. Sjåstad, Solid State Ionics **305**, 7 (2017).
[29] J. Bassat, C. Allançon, P. Odier, J. Loup, M. D. Carvalho, and A. Wattiaux, Eur. J. Solid State Inorg. Chem. **35**, 173 (1998).
[30] A. Olafsen, H. Fjellvåg, and B. C. Hauback, J. Solid State Chem. **151**, 46 (2000).
[31] Y. Sakurai, N. Chiba, Y. Kimishima, and M. Uehara, Physica C: Superconductivity **487**, 27 (2013).

[32] Z. Zhang and M. Greenblatt, J. Solid State Chem. **117**, 236 (1995).
[33] P. A. Lee and T. V. Ramakrishnan, Rev. Mod. Phys. **57**, 287 (1985).
[34] K. Sreedhar, M. McElfresh, D. Perry, D. Kim, P. Metcalf, and J. Honig, J. Solid State Chem. **110**, 208 (1994).
[35] Y. Kobayashi, S. Taniguchi, M. Kasai, M. Sato, T. Nishioka, and M. Kontani, J. Phys. Soc. Jpn. **65**, 3978 (1996).
[36] G. Wu, J. J. Neumeier, and M. F. Hundley, Phys. Rev. B **63**, 245120 (2001).
[37] S. Rosenkranz, M. Medarde, F. Fauth, J. Mesot, M. Zolliker, A. Furrer, U. Staub, P. Lacorre, R. Osborn, R. S. Eccleston *et al.*, Phys. Rev. B **60**, 14857 (1999).
[38] M. Freamat, X. N. Lin, V. Durairaj, S. Chikara, G. Cao, and J. W. Brill, Phys. Rev. B **72**, 014458 (2005).
[39] F. Bartolomé, M. Kuz'min, J. Bartolomé, J. Blasco, J. García, and F. Sapina, Solid State Commun. **91**, 177 (1994).
[40] C. Y. Ho and R. E. Taylor, *Thermal Expansion of Solids* (ASM International, 1998), Vol. 4.
[41] R. Klingeler, J. Geck, R. Gross, L. Pinsard-Gaudart, A. Revcolevschi, S. Uhlenbruck, and B. Büchner, Phys. Rev. B **65**, 174404 (2002).
[42] P. Gegenwart, Rep. Prog. Phys. **79**, 114502 (2016).
[43] R. Klingeler, J. Geck, S. Arumugam, N. Tristan, P. Reutler, B. Büchner, L. Pinsard-Gaudart, and A. Revcolevschi, Phys. Rev. B **73**, 214432 (2006).
[44] R. M. Fernandes, L. H. VanBebber, S. Bhattacharya, P. Chandra, V. Keppens, D. Mandrus, M. A. McGuire, B. C. Sales, A. S. Sefat, and J. Schmalian, Phys. Rev. Lett. **105**, 157003 (2010).
[45] We have applied the Clausius-Clapeyron equation and used $\Delta S = 2.8$ J/(mol K) as reported in Ref. [13].
[46] L. Wang, U. Köhler, N. Leps, A. Kondrat, M. Nale, A. Gasparini, A. de Visser, G. Behr, C. Hess, R. Klingeler *et al.*, Phys. Rev. B **80**, 094512 (2009).